CONTINUOUS SIMULATION OF A CONTINUOUS-DISCONTINUOUS FIBER-REINFORCED THERMOPLASTIC (CODICOFRTP) COMPRESSION MOLDING PROCESS

L. Schreyer[1*], B. Scheuring[2], N. Christ[2,3], J. Blarr[2], C. Krauß[1], W. V. Liebig[2], K. A. Weidenmann[4], T. Böhlke[5], A. Hrymak[6], L. Kärger[1]

[1] Institute of Vehicle Systems Technology (FAST) – Digitization in Lightweight Design, Karlsruhe Institute of Technology (KIT), Karlsruhe, Germany
[2] Institute for Applied Materials, Karlsruhe Institute of Technology (KIT), Karlsruhe, Germany
[3] Fraunhofer Institute for Mechanics of Materials, Freiburg, Germany
[4] Institute of Materials Resource Management, University of Augsburg, Augsburg, Germany
[5] Institute of Engineering Mechanics, Karlsruhe Institute of Technology (KIT), Karlsruhe, Germany
[6] Department of Chemical and Biochemical Engineering, Western University, London, Canada
* Corresponding author (louis.schreyer@kit.edu)

Keywords: CAE chain, Co-molding simulation, LFT, Structural simulation, Mean-field homogenization

ABSTRACT

A virtual process chain for compression molded long fiber-reinforced thermoplastic (LFT) composites with co-molded continuous fiber-reinforced thermoplastics (CoFRTP) consisting of a compression molding and structural simulation step is established. The compression molding simulation considers the three-dimensional initial fiber orientation distribution of the semi-finished LFT plastificate and applies the Moldflow rotary diffusion (MRD) model to predict the reorientation of fibers. The predicted fiber orientations are compared to experimental results obtained from micro computed tomography (µCT) scans. The mapping step from molding to structural simulation allows the transfer of higher order anisotropy. Challenges in homogenizing the effective elastic material behavior of the direct (D-) LFT are discussed. The structural simulation is validated by means of coupon-level four-point bending tests on a D-LFT tape sandwich. The predicted bending stiffness shows higher accuracy if the mapped fiber orientation data are considered.

1 INTRODUCTION

Compression molded discontinuous fiber-reinforced thermoplastics (DiCoFRTP) have become well-established engineering materials due to their high specific strength and stiffness, short cycle times, and a high degree of design freedom. Regarding stricter environmental requirements and due to their superior recycling properties compared to thermosets, DiCoFRTP are increasingly being used, e.g., in the automotive sector. However, these materials are mostly restricted to semi-structural components because of the intrinsic fiber discontinuity. A possibility to overcome this deficiency is to hybridize DiCoFRTP with co-molded CoFRTP. The hybridization introduces tailored local load-bearing structures in critically loaded areas to strengthen and stiffen the component.

As the pressure to reduce costs and shorten development cycles increases, virtual process chains have become a powerful tool in product development. These digital twins depict a holistic simulation approach with forward transfer of all relevant process parameters and process results. Virtual process chains were already established for discontinuous fiber-reinforced polymers (DiCoFRP) in [1-4] and for CoFRPs in [5-7]. For DiCoFRTP, the virtual process chain usually consists of the steps molding, warpage, and structural simulation. Since the final fiber orientation distribution of DiCoFRTP is determined during the flow, virtual process chains are of utmost interest for these material systems, as shown by Buck et al. [8] for D-LFT. The hybridization with CoFRTP introduces additional complexity to the individual simulation steps. For instance, the final adhesion between the CoFRTP and the DiCoFRTP strongly depends on molding parameters. Further, depending on the component geometry

L. Schreyer, B. Scheuring, N. Christ, J. Blarr, C. Krauß, W. V. Liebig, K. A. Weidenmann, T. Böhlke, A. Hrymak, L. Kärger

and the positioning of the CoFRTP, the CoFRTP forming process must also be considered in the process simulation.

In this study, we present a virtual process chain for compression molded D-LFT with co-molded CoFRTP reinforcement. The digital twin features a compression molding simulation and a structural simulation, both of which are validated with experimental data. Additionally, we propose a method to transfer relevant process results. To highlight the significance of considering the fiber orientation distribution resulting from molding, we conduct additional structural simulations with various meaningful DiCoFRTP fiber orientation distributions. The authors point out that the focus of this contribution lies on the development and implementation of the described virtual process chain. However, effects that are not well captured by the models are discussed, and indicators for further investigations are suggested.

2 PROCESS AND MATERIAL

In D-LFT compression molding, the fibers are impregnated in line with the thermoplastic matrix during compounding and plastification by a twin-screw extruder setup. At the same time, the CoFRTP is heated in a contact oven and then co-molded with the D-LFT plastificate. The hand-held mold transfer and stacking of the individual semi-finished composites during molding are done sequentially. The layup configuration of the tapes is $[0°, 0°]$ and the layup thickness is 0.22 mm. The CoFRTP and the D-LFT consist of identical fiber and matrix material, namely carbon fiber-reinforced polyamide 6 (CF-PA6). Table 1 and Table 2 list the material properties of the D-LFT and the CoFRTP, respectively. The fiber length and the mean fiber volume content of the D-LFT are determined from nine evenly spread (25×25) mm² samples of a molded $(400 \times 400 \times 3)$ mm³ D-LFT plate. The fiber length is given by the number average $L_{\mathrm{n}} = \sum_{i=0}^{m} l_i \mathrm{n}_i / \sum_{j=0}^{m} \mathrm{n}_j$, where l_i is the fiber length and n_i the corresponding number of fibers of the i-th length cluster.

Property	LFT	Matrix	Fiber
Mean fiber volume content	$\bar{\varphi} = 23.6 \pm 1.4\,\%$		
Number-average fiber length	$L_{\mathrm{n}} = 1.5$ mm		
Fiber diameter			$d_{\mathrm{f}} = 7.2\,\mu\mathrm{m}$
Young's modulus		$E_{\mathrm{m}} = 3.1$ GPa	$E_{\mathrm{f},11} = 242.0$ GPa
Poisson's ratio		$\nu_{\mathrm{m},12} = 0.39$	

Table 1: Material properties of the CF-PA6 D-LFT material and its constituents.

Property	Tape
Fiber volume content	$\varphi = 48.0\,\%$
Mass density	$\rho = 1.48 \cdot 10^3$ kg m^{-3}
Young's modulus (longitudinal direction)	$E_{11} = 91.75$ GPa
Young's modulus (transverse direction)*	$E_{22} = 6.36$ GPa
In-plane shear modulus*	$G_{12} = 2.80$ GPa
Poisson's ratio**	$\nu_{12} = 0.297$
Heat capacity [9]	$c_{\mathrm{p}} = 2.0 \cdot 10^3$ J kg^{-1} K^{-1}
Heat transfer coeff. (free convection) [9]	$h_{\mathrm{c}} = 8.0$ W m^{-2} K^{-1}
Heat transfer coeff. (forced convection) [9]	$h_{\mathrm{fc}}(v = 3$ m s$^{-1}) = 325.0$ W m^{-2} K^{-1}
Heat transfer coeff. (mold-ply) [9]	$h_{\mathrm{mold}} = 1.05 \cdot 10^3$ W m^{-2} K^{-1}

* Approximated using the semi-empirical Halpin Tsai homogenization [10].
** Approximated using the rule of mixture.

Table 2: Material properties of CF-PA6 tape "TECHNYL LITE C130 C60" from DOMO.

3   METHODOLOGY

A co-molded D-LFT tape sandwich with dimensions $(400 \times 400 \times 2.95)\,\text{mm}^3$ serves as a demonstrator to validate the results of the virtual process chain by means of experimental four-point bending tests following DIN ISO 14125. Figure 1 illustrates the individual steps of the virtual process chain.
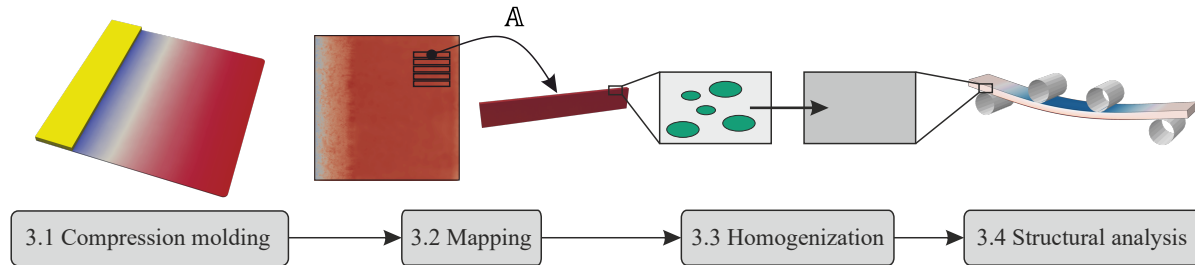
Figure 1: Schematic of the virtual process chain.

3.1 COMPRESSION MOLDING SIMULATION

The flow behavior of D-LFT is shear-dominated resulting from a thin solidified layer at the mold surface. This arises from the high heat dissipation at the cold mold surface and the low thermal conductivity of the D-LFT. Therefore, the tangential fluid velocity at the mold surface is zero corresponding to a no-slip boundary condition. When co-molding tapes, the question arises as to whether the assumption of a no-slip condition between the D-LFT and CoFRTP is feasible as well. This contact surface interaction mainly depends on the tape's temperature and the convective heat transfer with the D-LFT. The CoFRTP cools during the mold transfer and the residence time in the mold until the press motion is triggered. The convective heat transfer coefficient at the mold surface is high compared to the free and forced convective heat transfer coefficients (compare Table 2). However, forced convection has a high cooling effect for higher air stream velocities as shown by Dörr [9]. An analytical approximation of the homogeneous tape temperature $\bar{T}$ is obtained by solving the one-dimensional heat equation with convective heat transfer,

$$\rho c_{\text{p}} V \frac{d\bar{T}}{dt} = h_s A(\bar{T}_0 - T_s),$$

(1)

where h_s and T_s are the heat transfer coefficient and the Temperature of the convective or conductive heat sink, respectively. Figure 2 shows the corresponding solution for free convection, forced convection and convective heat transfer between the CoFRTP and the mold, using the heat transfer coefficients listed in Table 2, and the aforementioned CoFRTP thickness. The temperature of the mold and the ambient temperature are $T_{\text{mold}} = 80\,°\text{C}$ and $T_{\text{air}} = 25\,°\text{C}$, respectively. We note that manual process handling does not match the velocity of an industrial robot, which is around $3\,\text{m s}^{-1}$ and which was the basis for the heat transfer measurements. However, the results highlight the strong influence of the CoFRTP handling on the temperature. Due to the small thickness of the CoFRTP and high heat flow when interacting with the mold surface, we assume the bottom CoFRTP layup to have the same temperature and to behave as the mold surface during the compression molding simulation. However, the upper tape has no contact surface with the mold prior to the flow phase during molding. Due to the small thickness of the tape layup and the manual tape handling, the upper tape cools by convection below the crystallization temperature during the transfer and placement in the mold. Moreover, the D-LFT plastificate's surface cools below the crystallization temperature until the upper CoFRTP is placed on top, which prevents the upper tape from reheating. Therefore, we make the broad assumption to model both CoFRTPs as mold surfaces, i.e., assume no-slip condition and mold temperature.

L. Schreyer, B. Scheuring, N. Christ, J. Blarr, C. Krauß, W. V. Liebig, K. A. Weidenmann, T. Böhlke, A. Hrymak, L. Kärger
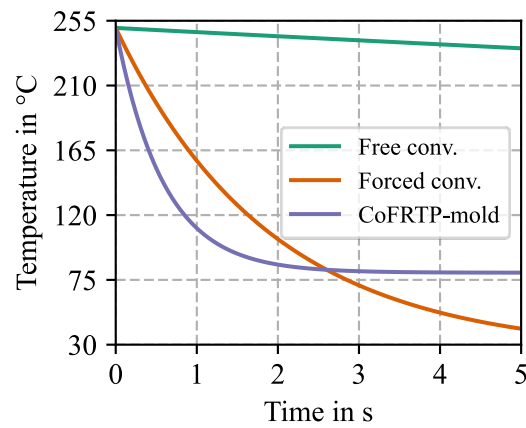
Figure 2: Analytical approximation of CoFRTP cooling for free convection, forced convection ($v = 3 \text{ m s}^{-1}$) and convective heat transfer at the mold surface.

The compression molding simulation is performed with AUTODESK MOLDFLOW 2023 using an isotropic viscosity approach. The plate is meshed with tetrahedral elements with a global mesh size of $l_e = 5$ mm, a refined mesh size of $l_e = 3$ mm in the plastificate region, and 16 elements through the thickness (see Figure 3a). The dimensions of the plastificate are $(82 \times 400 \times 13) \text{ mm}^3$ discretized with $l_e = 1$ mm tetrahedral elements. The three-dimensional initial fiber orientation distribution of the plastificate is approximated by the geometric-based approach introduced by Schreyer et al. [11]. Figure 3b shows the initial fiber orientation distribution of the plastificate through a section in the x-z-plane. The fiber orientation tensors are rendered as superquadratic glyphs [12]. The fibers in the outermost element layer are fully aligned in extrusion (y-) direction, and therefore are not visible.

(a)   (b)
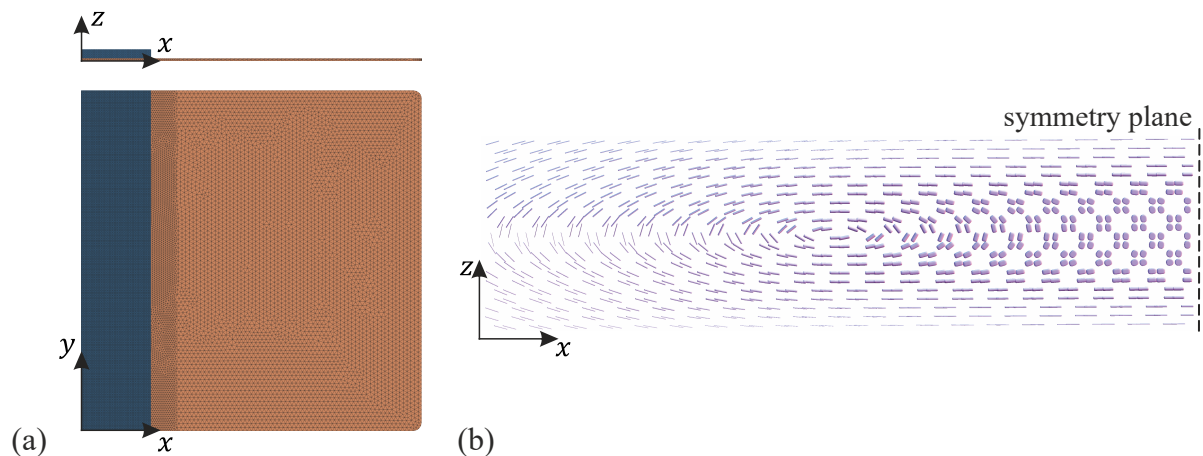
Figure 3: (a) Process simulation model consisting of the plastificate (blue) and the plate (orange) and (b) initial fiber orientation of a half section through the x-z-plane of the plastificate represented as superquadratic tensor glyphs.

The reorientation of fibers is modeled by the MRD model [13] using the fiber interaction coefficient $C_i = 0.0015$. The rotational diffusion model coefficients are $D_1 = 1.0$, $D_2 = 0.5$ and $D_3 = 0.3$. The fourth-order fiber orientation tensor $\mathbb{A}$ is approximated by the Moldflow Bi-quadratic closure approximation based on Cintra and Tucker [14].

3.2 MAPPING OF FIBER ORIENTATION DISTRIBUTION

In the context of DiCoFRP, the local fiber orientation distribution, which establishes during the flow phase of compression molding, significantly determines the mechanical properties. Because the element size and/or element type changes between the compression molding and structural simulation model, an intermediate mapping step is mandatory [15]. A comprehensive overview of interpolation methods and their applicability in the context of virtual process chains of FRPs is given by Krauß et al. [16]. To account for higher-order anisotropy, we interpolated the fourth-order fiber orientation tensor $\mathbb{A}$, which is needed further on for stiffness homogenization. Because the fiber orientation distribution is described by the second-order tensor during compression molding, the IBOF closure is utilized to approximate the fourth-order fiber orientation tensor on the molding simulation mesh. The interpolation is done component-wise by a tensorial extension of the Euclidean interpolation method [16]:

$$\bar{A}_{ijkl} = \sum_{m}^{N} w_m A_{m,ijkl}.$$ (2)

The inverse distance method as introduced by Shepard [17] choosing the power parameter $p = 2$ and the $N = 4$ nearest neighbors is used to determine the weights w_m:

$$w_m = \frac{1}{\|x_m - x\|} \frac{1}{\sum_{j}^{N} \|x_j - x\|^{-p}}.$$ (3)

This approach seems reasonable because there are no significant gradients in the resulting fiber orientation tensor field. However, the authors note, that orthotropic tensor properties, which are introduced by the IBOF closure, are not generally preserved by the Euclidean interpolation method.

3.3 HOMOGENIZATION OF THE DICO COMPOSITE

The effective elastic composite properties of the D-LFT are computed by the mean-field homogenization method of Tandon and Weng [18], which is derived from Mori and Tanaka's approach [19]. Tandon and Weng propose explicit equations to compute the effective properties of discontinuous fiber-reinforced composites for fully aligned fibers. However, the equation for the plane-strain bulk modulus k_{23} and the Poisson's ratio ν_{12} must be solved iteratively. To avoid an iterative solution procedure, we used the explicit formulation given by Tucker [20]. The model by Tandon and Weng assumes isotropic constituents, and the fibers to behave as if they are embedded in an infinite elastic matrix. The microstructure is described by the fiber volume fraction φ and the fiber aspect ratio r. Figure 4 shows the dependency of the effective tensile modulus in longitudinal and transverse direction $\bar{E}_{11}$ and $\bar{E}_{22}$, the effective in-plane shear modulus $\bar{G}_{12}$ and the in-plane Poisson's ratio $\bar{\nu}_{12}$ on the fiber aspect ratio r. For comparison, the Mori and Tanaka estimate following Benveniste [21] using [22] is plotted as well. The orientation-dependent effective stiffness tensor $\bar{\mathbb{C}}(\mathbb{A})$ is computed according to the orientation averaging scheme by Advani and Tucker [23].

3.4 STRUCTURAL SIMULATION

The structural simulations of the four-point bending test are conducted using the finite element software ABAQUS 2021.HF14. Figure 5 shows the schematic and numerical model of the four-point bending test. The $(100 \times 15 \times 2.95)$ mm^3 CoDiCoFRTP specimen is modeled using a continuum mechanics approach with fully integrated quadratic hexahedrons C3D20 with an edge length of $l_e = 1$ mm in the x-y-plane. In the z-direction, the CoFRTP and D-LFT are meshed with 2 and 12 elements, respectively. The support and loading rollers are modeled as analytical rigid bodies neglecting friction. The loading of $u_z = -1$ mm is applied in a static step with automatic stabilization with a dissipated energy fraction of $0.2 \cdot 10^{-3}$ to increase the numerical stability. To fully constrain the model, the displacements u_x, u_y and the rotation around the z-axis u_{rz} of the center node of the top surface are constrained.

L. Schreyer, B. Scheuring, N. Christ, J. Blarr, C. Krauß, W. V. Liebig, K. A. Weidenmann, T. Böhlke, A. Hrymak, L. Kärger
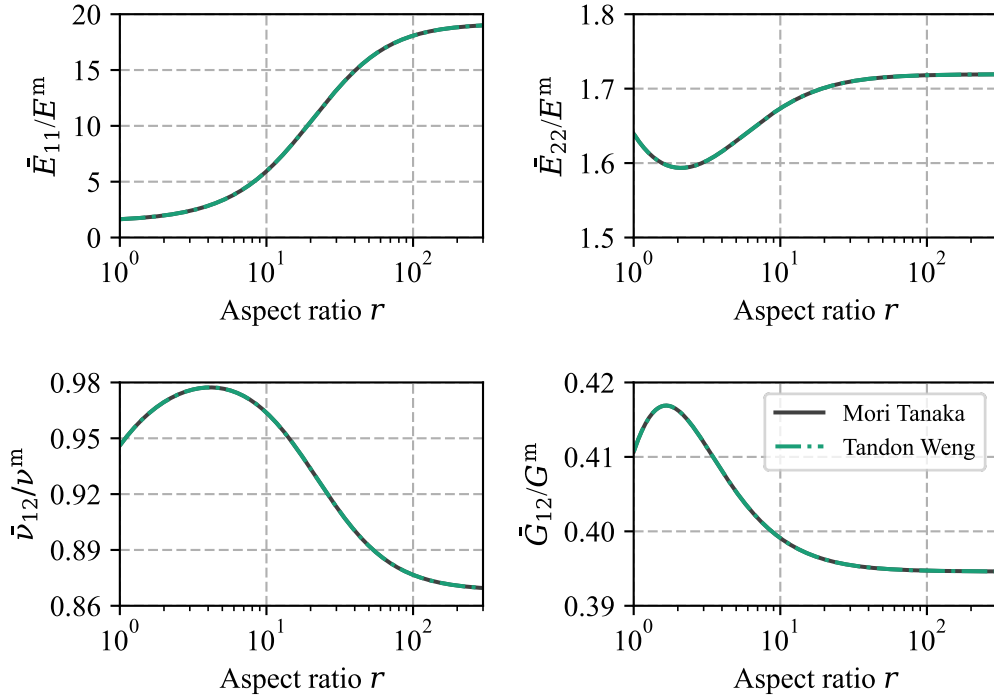
Figure 4: Influence of the fiber aspect ratio on effective engineering constants $\bar{E}_{11}$, $\bar{E}_{22}$, $\bar{G}_{12}$ and $\bar{\nu}_{12}$ according to the homogenization methods of Tandon and Weng [18] and Mori and Tanaka following Benveniste [21] for fully aligned fibers in the 1-direction.
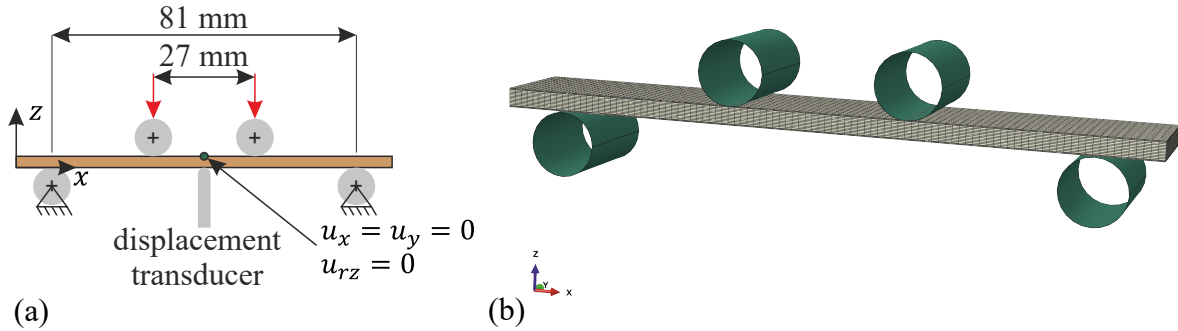
Figure 5: (a) Schematic of the four-point bending setup and (b) the corresponding finite element model.

The mechanical properties of the D-LFT are determined according to the mapping and homogenization approaches introduced in Sections 3.2 and 3.3.

The mechanical properties of the CoFRTP are listed in Table 2. The Young's modulus E_{11} is determined following DIN ISO 527-4, whereas the remaining engineering constants are estimated analytically. However, the load case introduces mainly uniaxial compressive and tensile stress in the CoFRTP layers. The Poisson's ratio ν_{12} is approximated following the rule of mixture $\nu_{12} = \nu_{f,12}\varphi + \nu_{m,12}(1 - \varphi)$ using $\nu_{f,12} = 0.2$. The semi-empirical Halpin-Tsai model [10] choosing the fitting parameter $\xi = 2$ is used to approximate the transverse modulus E_{22} and the in-plane shear

modulus G_{12}. The corresponding equation to compute the effective composite property $(\cdot)$ from the fiber and matrix property $(\cdot)_\text{f}$ and $(\cdot)_\text{m}$ reads as follows:

$$(\cdot) = (\cdot)_\text{m} \frac{1 + \xi\eta\varphi}{1 - \eta\varphi}, \qquad \eta = \frac{(\cdot)_\text{f} - (\cdot)_\text{m}}{(\cdot)_\text{f} + \xi(\cdot)_\text{m}}. \tag{6}$$

The fiber properties $E_{\text{f},22} = 14.0$ GPa and $G_{\text{f},12} = 8.78$ GPa of a T800S fiber are taken from Duan et al. [24]. The out-of-plane shear modulus G_{23} is roughly estimated using $G_{23} = 2/3\ G_{12}$ because the four-point bending test does not introduce significant out-of-plane shear deformation within the CoFRP layers.

4   RESULTS AND DISCUSSION

4.1 VALIDATION OF THE PROCESS SIMULATION

We validated the fiber orientation model by comparing the resulting fiber orientation of the compression molding simulation with experimental results of a 3 mm thick CF-PA6 D-LFT plate with lateral plastificate positioning. The experimental fiber orientation tensors are estimated from µCT scans from $(25 \times 25 \times 3)$ mm^3 cut-outs by applying the algorithm of the gradient-based approach by Pinter et al. [25] adjusting the pre-filtering for carbon fiber scans. The locations of these samples are shown in Figure 6b. For comparability with experimental data, the simulative fiber orientation tensors are averaged over the thickness. Averaging does not yield a more isotropic orientation distribution because the experimental and simulation results do not show a significant shell-core effect in the flow region. Figure 6a shows the projections of the orbital plots $p = An$ of the second-order fiber orientation tensor A onto the x-y- and x-z-plane in the global coordinates. Here, n is a unit vector. The experimental fiber orientation tensors A_1 and A_2 exhibit a rotation around the z-axis of 14.3° and 6.9°, although the cause is not yet fully understood. Possible explanations are geometric deviations between the plastificate ends introduced by the cutting unit or density fluctuations within the plastificate, which lead to an inclined flow front. The shape of the second-order fiber orientation tensors is validated using their eigenvalues λ_i, as shown in Figure 7. The experimental orientation tensors exhibit an almost ideally planar orientation state, whereas the simulation predicts a higher probability of fibers oriented in normal direction. The predicted and experimental Frobenius norms of the eigenvalues of the second-order fiber orientation tensor $\|\lambda\|_\text{F} = \sqrt{\sum_i \lambda_i^2}$ at the points of interest (POI) 1 and 2 are in good agreement deviating by 0.31 % and 6.15 %, respectively. The deviating rotation and shape of the experimental fiber orientation tensors is partly attributed to intrinsic process scatter, making µCT scans of several D-LFT plates necessary.
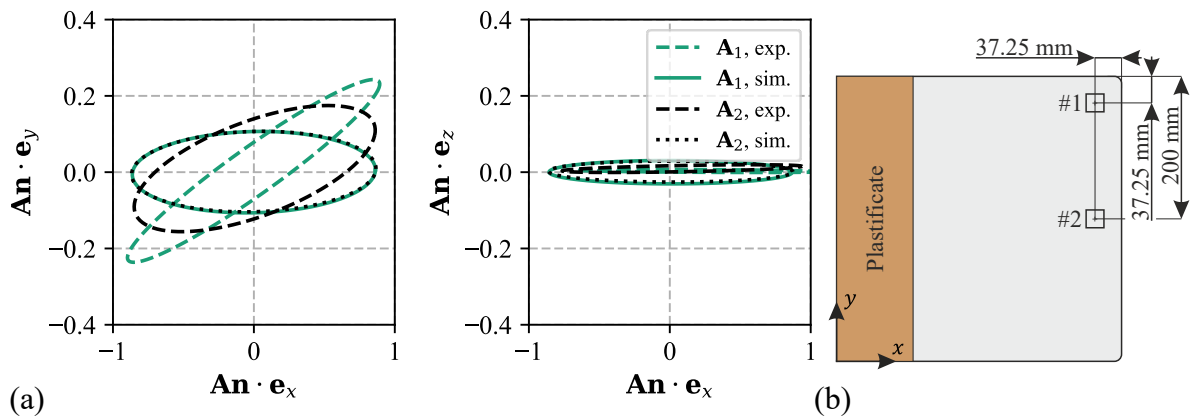
Figure 6: (a) Projections of experimental and simulative second-order fiber orientation tensor A_1 and A_2 at (b) points of interest (POI) 1 and 2 in the global coordinate system.

L. Schreyer, B. Scheuring, N. Christ, J. Blarr, C. Krauß, W. V. Liebig, K. A. Weidenmann, T. Böhlke, A. Hrymak, L. Kärger
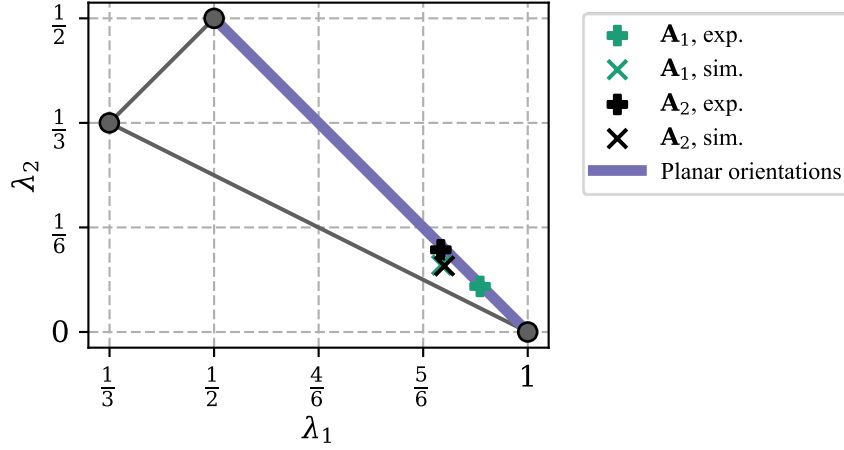
Figure 7: Eigenvalues λ_i of the experimental and simulative second-order fiber orientation tensors $\boldsymbol{A}_1$ and $\boldsymbol{A}_2$ at POI 1 and 2. The bounding lines span the admissible set of linear combinations of the eigenvalues λ_i, known as orientation triangle. The eigenvalues are sorted in descending order:
$$\lambda_1 \geq \lambda_2 \geq \lambda_3.$$

4.2 VALIDATION OF MEAN-FIELD HOMOGENIZATION

The mean-field homogenization results assuming the Poisson's ratio of the fiber $v_{f,12} = 0.2$ are compared to experimental results of D-LFT tension tests. The experiments are done following DIN ISO 527-4 for the orientations $(0, \pi/2)$ (see Figure 8b). The analytical results are given by the effective Young's modulus $\bar{E}(0, 2\pi)$ projected onto the x-y-plane according to

$$\bar{E}(\boldsymbol{d}) = \left((\boldsymbol{d}\otimes\boldsymbol{d}) \cdot \mathbb{C}^{-1}[\boldsymbol{d}\otimes\boldsymbol{d}]\right)^{-1}, \tag{4}$$

where $\boldsymbol{d}$ is a strain vector parametrized in spherical coordinates (θ, ψ) with $\|\boldsymbol{d}\| = 1$. Here, θ denotes the polar angle and ψ the azimuth angle. The experimental mean stiffness values are plotted as red dots in Figure 8a. Due to the in-line compounding, D-LFT exhibits a complex microstructure consisting of individual fibers and (split) bundles, whereas bundles tend to be longer than individual fibers. The naive approach, describing the microstructure by the experimental fourth-order fiber orientation tensors $\mathbb{A}_1$ and $\mathbb{A}_2$ (compare Figure 6), the average fiber volume content $\bar{\varphi}$ and the effective fiber aspect ratio $r \approx 208$ using the diameter of an individual fiber d_f and the number-average fiber length L_n (see Table 1), overestimates the effective composite behavior. Consequently, the microstructure descriptors of the Tandon and Weng homogenization should consider fiber bundles. The reverse parameter identification to fit the orientation averaged stiffness $\bar{\mathbb{C}}(\mathbb{A}_1)$ and $\bar{\mathbb{C}}(\mathbb{A}_2)$ of the experimental fiber orientation tensors $\mathbb{A}_1$ and $\mathbb{A}_2$, cf. Figure 6, to the results of the experimental tension tests for $\psi = 0°$ yields the aspect ratios $r(\mathbb{A}_1) = 32.8$ and $r(\mathbb{A}_2) = 19.9$ (see Figure 8a). Here, the experimental fiber orientation data is used because the molding simulation does not predict the rotation of the fiber orientation around the out-of-plane (z-) axis.

Estimating the effective fiber diameter by the linear weighting function

$$d_{\text{eff}} = w d_f + (1 - w) d_b \tag{5}$$

does not yield meaningful results because the ideal bundle diameter is $d_{b,\text{ideal}} = \sqrt{n} d_f = 1.61 \text{ mm} > L_n$, where $n = 10^5$ is the number of fibers of an intact bundle. Consequently, the experimental number-average fiber length L_n is not suited to estimate the effective fiber aspect ratio, but effective fiber lengths for single fibers and bundles must be determined. Then the aspect ratio might be calculated using a weighted interpolation function like Eq. 5. Because the investigation for a meaningful descriptor of the microstructure is ongoing, we used the aspect ratio $r(\mathbb{A}_2)$ of the reverse parameter identification for the structural simulations of the demonstrator.
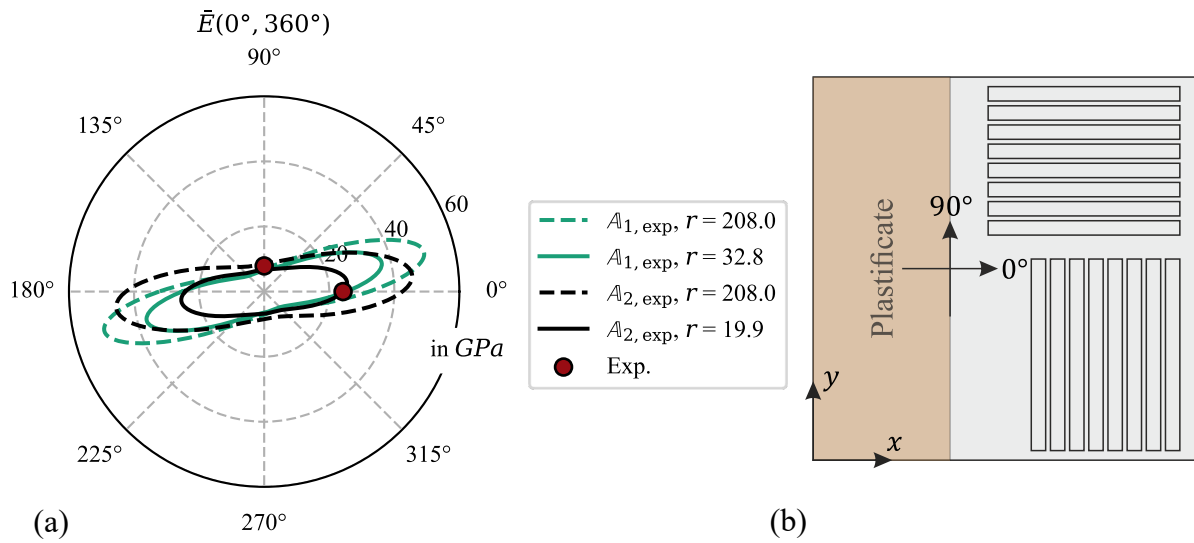
Figure 8: (a) Comparison of the experimental moduli with the effective elastic moduli $\bar{E}(0°, 360°)$ of the Tandon Weng homogenization projected onto the x-y-plane for the experimental fiber orientation distributions $\mathbb{A}_1$ and $\mathbb{A}_2$ at POI 1 and 2, cf. Figure 6b, and different fiber aspect ratios r. (b) Cutting plan of tension test samples and definition of orientation.

4.3 VALIDATION OF FOUR-POINT BENDING TEST

Figure 9a shows the resulting effective bending stiffness $\bar{E}_b$ of the CoDiCoFRTP of the four-point bending tests following DIN ISO 14125. The experimental result is shown as a boxplot. The results of the virtual specimens are plotted as dots. Figure 9b shows the cutting plan of the physical and virtual specimens. The virtual realizations with assumed constant fiber orientation states throughout the D-LFT constituent showcase the importance of considering the fiber orientation distribution from manufacturing. The upper and lower limit of possible effective bending stiffnesses when variating the fiber orientation are marked by the uniaxial fiber orientation states $A_{xx} = 1$ and $A_{yy} = 1$, respectively. The effective bending stiffness is underestimated in simulations that assume isotropic ($A_{ii} = 1/3$) and planar isotropic ($A_{xx} = A_{yy} = 0.5$) orientation states due to the neglected pronounced fiber orientation in the flow direction which develops during the flow phase of compression molding. The virtual specimens with mapped fiber orientations exhibit the most accurate results. The slight overestimation of the effective bending stiffness is attributed to the inclined flow front observed in the experiments. However, we want to emphasize that these results are obtained by using a fitted fiber aspect ratio for the Tandon Weng homogenization method. Minor deviations of the resulting fiber orientation of the molding simulation are amplified by the mapping procedure yielding slight scatter in the effective bending stiffness of the virtual specimen with mapped fiber orientation.

5 CONCLUSION

A virtual process chain for co-molded D-LFT is successfully established. The process chain consists of the essential steps compression molding simulation and structural simulation. An intermediate mapping step enables the transfer of higher order anisotropy by component-wise mapping of the spatial fourth-order fiber orientation tensor distribution. Four-point bending tests on cut-outs of a co-molded D-LFT tape sandwich served as a demonstrator for validation.

µCT scans on D-LFT plates show a high planar orientation of the fibers, motivating the consideration of the local fiber orientation in the design of CoDiCoFRTP components. The compression molding simulation which takes the three-dimensional initial fiber orientation and the Moldflow rotary diffusion model into account, predicts the resulting degree of anisotropy of the fibers well. However, the resulting fiber orientation in the flow region exhibits a rotation around the out-of-plane (z-) axis, whose cause needs further investigation.

L. Schreyer, B. Scheuring, N. Christ, J. Blarr, C. Krauß, W. V. Liebig, K. A. Weidenmann, T. Böhlke, A. Hrymak, L. Kärger
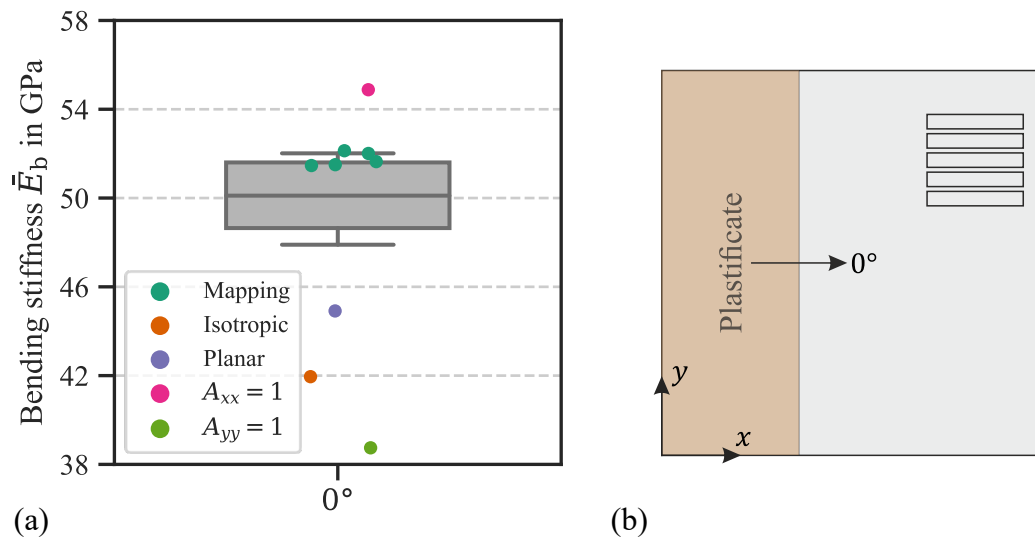
Figure 9: (a) Effective bending stiffness $\bar{E}_\mathrm{b}$ as predicted for different fiber orientation distributions by the simulation and as measured by experiments. (b) Cutting plan of the physical and virtual bending test specimens with mapped fiber orientation.

The significant influence of the CoFRTP handling prior to co-molding is demonstrated by means of an analytical approximation of the heat transfer. Due to the small thickness of the CoFRTP layup and the time-intensive manual handling, the CoFRTP is assumed to behave temperature-wise like the mold surface in the compression molding simulation of the demonstrator.

Virtual four-point bending specimens with mapped fiber orientation data from the compression molding simulation reproduce the physical bending stiffness most accurately. However, the complex microstructure of D-LFT includes a combination of fibers and fiber bundles. Approximating this microstructure by the number-average fiber length and single-fiber diameter in order to estimate the effective stiffness through mean-field homogenization methods based on Mori and Tanaka's method leads to overestimation. Due to the focus of this work on the virtual process chain, the homogenized material properties are determined by reverse parameter identification. To accurately evaluate these homogenization methods, a more detailed description of the microstructure must be developed. Because this paper solely investigates mean-field homogenization methods derived from Mori and Tanaka's method, other methods from the literature should be evaluated in the future.

The virtual process chain can be extended by damage modeling of the D-LFT to improve the prediction of the structural performance. Further enhancements include the delamination between the CoFRTP and the DiCoFRTP, the transfer of varying fiber volume contents and an anisotropic viscosity model to accurately capture the influence of the fibers on the flow behavior. The consideration of eigenstresses which result from inhomogeneous cooling can be incorporated to improve the accuracy of the structural simulation. Here, the heat transfer between the CoFRTP and the DiCoFRTP must be considered.

ACKNOWLEDGEMENTS

CONTRIBUTIONS

LS was responsible for the development of the methodology presented in this publication. CK and LS developed and implemented the mapping procedure. LS developed the compression molding and

structural simulation models. NC implemented the Mori and Tanaka homogenization method. Conceptualization and establishment of the process chain was taken over by LS. BS carried out the experiments. JB performed µCT analysis and developed the method to determine the fiber orientations. Validation, investigation of the results, formal analysis and the subsequent visualization were performed by LS. The original manuscript draft was written by LS and extensively reviewed and edited by all authors. The research was supervised by WVL, KW, TB, AH and LK.

REFERENCES

[1]   C. A. Reclusado, S. Nagasawa, Modeling of fiber-reinforced plastics taking into account the manufacturing process, *Proceedings of the VII European Congress on Computational Methods in Applied Sciences and Engineering (ECCOMAS Congress 2016)*, Athens, Greece, 2016, pp 2220–2235. (https://doi.org/10.7712/100016.1955.5840)

[2]   J. Görthofer, N. Meyer, T.D. Pallicity, L. Schöttl, A. Trauth, M. Schemmann, M. Hohberg, P. Pinter, P. Elsner, F. Henning, A. N. Hrymak, T. Seelig, K. Weidenmann, L. Kärger, T. Böhlke, *Virtual process chain of sheet molding compound: Development, validation and perspectives*, Composites Part B: Engineering, **169**, 2019, pp 133–147. (https://doi.org/10.1016/j.compositesb.2019.04.001)

[3]   N. Meyer, S. Gajek, J. Görthofer, A. Hrymak, L. Kärger, F. Henning, M. Schneider, T. Böhlke, *A probabilistic virtual process chain to quantify process-induced uncertainties in Sheet Molding Compounds*. Composites Part B: Engineering, **249**, 2023, 110380. (https://doi.org/10.1016/j.compositesb.2022.110380)

[4]   V. Romanenko, M. Duhovic, D. Schommer, J. Hausmann, J. Eschl, *Advanced process simulation of compression molded carbon fiber sheet molding compound (C-SMC) parts in automotive series applications*, Composites Part A: Applied Science and Manufacturing, **157**, 2022. (https://doi.org/10.1016/j.compositesa.2022.106924)

[5]   L. Kärger, A. Bernath, F. Fritz, S. Galkin, D. Magagnato, A. Oeckerath, A. Schön, F. Henning *Development and validation of a CAE chain for unidirectional fibre reinforced composite components*, Composite Structures, **132**, 2015, pp 350–358. (https://doi.org/10.1016/j.compstruct.2015.05.047)

[6]   L. Kärger, S. Galkin, C. Zimmerling, D. Dörr, J. Linden, A. Oeckerath, K. Wolf, *Forming optimisation embedded in a CAE chain to assess and enhance the structural performance of composite components*, Composite Structures, **192**, 2018, pp 143–152. (https://doi.org/10.1016/j.compstruct.2018.02.041)

[7]   N. Mayer, J. Prowe, T: Havar, R. Hinterhölzl, K. Drechsler, *Structural analysis of composite components considering manufacturing effect*, Composite Structures, **140**, 2016, pp 776–782. (https://doi.org/10.1016/j.compstruct.2016.01.023)

[8]   F. Buck, B. Brylka, V. Müller, T. Müller, K. A. Weidenmann, A. N. Hrymak, F. Henning, T. Böhlke, *Two-scale structural mechanical modeling of long fiber reinforced thermoplastics*, Composites Science and Technology, **117**, 2015, pp 159–167. (https://doi.org/10.1016/j.compscitech.2015.05.020)

[9]   D. Dörr, *Simulation of the thermoforming process of UD fiber-reinforced thermoplastic tape laminates*, Dissertation, Karlsruhe University of Technology (KIT), 2019. (https://doi.org/10.5445/KSP/1000099858)

[10]   J.C.H. Affdl, J.L. Kardos, *The Halpin-Tsai equations: A review*, Polymer Engineering & Science, **16**(5), 1976, pp 344–352. (https://doi.org/10.1002/pen.760160512)

[11]   L. Schreyer, J. Blarr, K. Höger, N. Meyer, L. Kärger, *Generation of initial fiber orientation states for long fiber reinforced thermoplastic compression molding simulation,* 20th European Conference on Composite Materials (ECCM 2022), Lausanne, Switzerland, 2022, pp 687–694. (https://doi.org/10.5445/IR/1000155599)

[12]   T. Schultz, G.L. Kindlmann, *Superquadric Glyphs for Symmetric Second-Order Tensors*, IEEE Transactions on Visualization and Computer Graphics, **16**(6), 2010, pp 1595–1604. (https://doi.org/10.1109/TVCG.2010.199)

[13]   A. Bakharev, H. Yu, S. Ray, R. Speight, J. Wang, *Using New Anisotropic Rotational Diffusion Model to Improve Prediction of Short Fibers in Thermoplastic Injection Molding*, ANTEC: Orlando, FL, USA, 2018.

[14]   J.S. Cintra, C.L. Tucker, *Orthotropic closure approximations for flow-induced fiber orientation*. Journal of Rheology, **39**(6), 1995, pp 1095–1122. (https://doi.org/10.1122/1.550630)

[15]   N. Mayer, B. van den Broucke, J. Prowe, T. Havar, R. Hinterhölzl, *Finite element mapping for incompatible FE meshes of composite structures*. Advances in Engineering Software, **99**, 2016, pp 81–88. (https://doi.org/10.1016/j.advengsoft.2016.05.007)

[16]   C. Krauß, L. Kärger, *Tensor interpolation in virtual manufacturing chains for fiber reinforced composites*. International Journal of Mechanical Sciences, **226**, 2022, 107378. (https://doi.org/10.1016/j.ijmecsci.2022.107378)

[17]   D. Shepard, *A two-dimensional interpolation function for irregularly-spaced data*, Proceedings of the 23rd ACM National Conference, 1968, pp 517–524. (https://doi.org/10.1145/800186.810616)

[18]   G. P. Tandon, G.J. Weng, *The effect of aspect ratio of inclusions on the elastic properties of unidirectionally aligned composites*, Polymer Composites, **5**(4), 1984, pp 327–333. (https://doi.org/10.1002/pc.750050413)

[19]   T. Mori, K. Tanaka, *Average stress in matrix and average elastic energy of materials with misfitting inclusions*, Acta Metallurgica, **21**(5), 1973, pp 571–574. (https://doi.org/10.1016/0001-6160(73)90064-3)

[20]   C.L. Tucker III, E. Liang, *Stiffness predictions for unidirectional short-fiber composites: Review and evaluation*, Composites Science and Technology, **59**(5), 1999, pp 655–671. (https://doi.org/10.1016/S0266-3538(98)00120-1)

[21]   Y. Benveniste, *A new approach to the application of Mori-Tanaka's theory in composite materials*, Mechanics of Materials, **6**(2), 1987, pp 147–157. (https://doi.org/10.1016/0167-6636(87)90005-6)

[22]   N. Christ, *Extraweich/homopy: v1.0.11 (1.0.11)*, Zenodo, 2023. (https://doi.org/10.5281/zenodo.7967631)

[23]   S. G. Advani, C. L. Tucker, *The Use of Tensors to Describe and Predict Fiber Orientation in Short Fiber Composites*, Journal of Rheology, **31**(8), 1987, pp 751–784. (https://doi.org/10.1122/1.549945)

[24]   S. Duan, F. Liu, T. Pettersson, C. Creighton, L.E. Asp, *Determination of transverse and shear moduli of single carbon fibres*. Carbon, **158**, 2020, pp 772–782. (https://doi.org/10.1016/j.carbon.2019.11.054)

[25]   P. Pinter, S. Dietrich, B. Bertram, L. Kehrer, P. Elsner, K.A. Weidenmann, *Comparison and error estimation of {3D} fibre orientation analysis of computed tomography image data for fibre reinforced composites*, NDT & E International, **95**, 2018, pp. 26–35. (https://doi.org/10.1016/j.ndteint.2018.01.001)